RSC Advances

PAPER

View Article Online
View Journal | View Issue

Cite this: *RSC Adv.*, 2020, **10**, 31070

Simultaneous tuning of optical and electrical properties in a multifunctional $LiNbO_3$ matrix upon doping with Eu^{3+} ions†

Nimai Pathak, *[a] Partha Sarathi Ghosh, [b] Sumanta Mukherjee[c] and Balaji Prasad Mandal [d]

Received 27th February 2020
Accepted 7th August 2020

DOI: 10.1039/d0ra01869d

rsc.li/rsc-advances

Combined photoluminescence (PL) and dielectric studies have been carried out on both undoped and Eu^{3+} doped $LiNbO_3$ compounds for their potential application in optical–electrical integration for the first time. Special focus has been given to simultaneously tuning both these physical properties. A PL study reveals that the blank compound is a blue emitting material, while upon doping with Eu^{3+} ions, the emitting color can be tuned from blue to red upon changing the excitation wavelength. Interestingly, the electrical property measurement of this ferroelectric compound showed that upon doping with Eu^{3+} ions, the remnant polarization was increased significantly. Density Functional Theory (DFT) based calculations were carried out to explain both the optical and electrical properties. It has been found that different defect centers are responsible for the bluish host emission while Eu^{3+} ions are energetically preferred to occupy the Nb site and gives rise to red emission. The DFT based results also showed that Eu^{3+} ions induced more distortion into the nearby Nb-site, which is responsible for enhancement of the remnant polarization. Stark-splitting patterns in the PL study also showed that the point symmetry of $LiNbO_3$ upon Eu^{3+} doping changes from C_{6v} to D_3, which indicates that the structure becomes less symmetric. Overall, the study presents a novel approach to designing multifunctional materials for optical–electrical integration application and to tuning their physical properties simultaneously in the desired range.

1. Introduction

Multifunctional materials are always considered as intelligent or smart materials, since they offer two or more desirable properties. For example, porous Si shows both fluorescent and semi-conductive properties, which makes it a preferable candidate for electro-optical integration applications.[1] Similarly, semiconductors doped with transition metal ions may exhibit both semiconducting and magnetic properties, which is very important for application in the field of spintronics.[2] Among the wide arrays of multifunctional materials, ferroelectric host materials always offer versatile applications; for example, there is the possibility of optical-electro-mechano or optical–electrical integration[3–5] when these materials are doped with rare earth ions, which results in many novel photoluminescence properties. Such electrical–optical integration can be the basis of many piezo-photonic devices, which have potential applications in e-signature systems, visible wearable electronics, *etc.*[6] Because of these multiple physical properties they have always been a hot research topic to the world's material researcher communities and new efforts are always being applied to the design and development of new multifunctional materials with controlled physical properties.

Presently, development of an environment friendly lead-free piezoelectric material has emerged as a hot research topic and niobate based compounds are found to be potential alternatives, and have a wide range of applications such as storage devices, sensors and generators.[7–9] Transition metal oxides such as the lithium niobates ($LiNbO_3$) are well known for their ferroelectric and optoelectronic properties.[10,11] The crystal structures of $LiNbO_3$ compounds consist of NbO_6 octahedra, which share corners. Although, the structure of $LiNbO_3$ (LNO) can be corelated to that of the ABO_3 perovskites[12,13], however the structure of LNO is different since Li^+ and Nb^{5+} ions have close ionic radii and both ions are placed in distorted octahedra surrounded by of six O^{2-} ions, unlike the A and B ions in perfect cubic ABO_3 perovskites. The formability of perovskite like structure for this compound is very less as discussed in earlier report by considering both Goldschmidt's tolerance factor t ($t = R_{A-O}/\sqrt{2}(R_{B-O})$, where R_{A-O} and R_{B-O} are A–O and B–O bond

[a]*Radiochemistry Division, Bhabha Atomic Research Centre, Mumbai, 400085, India. E-mail: nmpathak4@gmail.com; nimai@barc.gov.in; Fax: +91-22-25405151; Tel: +91-22-25590715 ext. 0636*

[b]*Glass and Advanced Materials Division, Bhabha Atomic Research Centre, Mumbai, 400085, India*

[c]*Fuel Chemistry Division, Bhabha Atomic Research Centre, Mumbai, 400085, India*

[d]*Chemistry Division, Bhabha Atomic Research Centre, Mumbai, 400085, India*

† Electronic supplementary information (ESI) available. See DOI: 10.1039/d0ra01869d

lengths in ABO_3 perovskie) and the octahedral factor. The t value for LNO is 0.75 which is beyond the stability range of 0.8–1.0. Thus the structure is highly distorted and such structural distortion in LNO is responsible for the ferroelectric behaviour.[14] In $NaNbO_3$, Johnston *et al.*, have demonstrated that the Nb^{5+} cations in NbO_6 octahedra have some positional disorder and they lies significantly off-center from the centrosymmetric positions toward an edge of the octahedron in a polar manner, in the "$P2_1ma$" polymorph.[15] Such off-center position of the Nb^{5+} ions is the main reason for ferroelectric behavior and thus structural distortion will have significant impact on this off-center position; more the distortion more will be the Nb^{5+} ions off-centered from their centrosymmetric positions. This will definitely have a notable impact on the ferroelectric properties.

One novel way to increase the distortion is to dope a different size cation and it was reported earlier that dopant ion such as Mg^{2+} (in the form MgO) can have significant impact on ferroelectric properties.[16] Further the vacancies are also found to have direct impact on the ferroelectric properties. Defect such as oxygen vacancies were recently reported to tune the dielectric behaviors.[17] These new defect centers may create new electronic states inside the band gap and gives rise to many interesting optical properties. In addition, if the dopant ion itself is a luminescent ion, such as rare earth ions, then along with the host emission, the dopant ion will also show its own characteristics emission. It has also been reported that upon doping with rare earth ion in a matrix such as strontium-barium niobate, there is a significant lowering of the ferroelectric phase transition T_c, which led to the enhancement of the dielectric permittivity and the decrease of the coercive field E_c.[18] This will help to develop a true piezo-photonic type material, where the luminescent dopant ion with different charges and sizes compared to the lattice ions may induce more structural distortion to control and tune the ferroelectric properties in addition to its own optical properties. Since a matrix like $LiNbO_3$ has two different lattice ions with different charges, the scope of tuning the physical properties is more by selectively doping the luminescent ions among the lattice sites. Such compounds with tuneable optical and electrical properties will be of great interest in the domain of multifunctional materials.

As far as rare earth doped LNO is concerned, doping with rare-earth ions (RE), such as Nd^{3+}, Yb^{3+} or Er^{3+}, impart the material as self-doubling laser material.[19–22] Among the lanthanides, Eu^{3+} ion has been used extensively for developing red phosphor after doping in suitable matrices, which can be excited by ultra violet (UV) light. Eu^{3+} ion also possess special characteristics such as (a) the intense emissions, which occurs from $^5D_0$ level do not split into sublevels in presence of crystal field, (b) the non-degenerate $^7F_0$ ground level and non-overlapping $^{2S+1}L_J$ multiplets and (c) the magnetic dipole (MD) transition ($^5D_0 \rightarrow {}^7F_1$) is usually the most intense one in a symmetrical crystal site while the electric dipole (ED) transition ($^5D_0 \rightarrow {}^7F_2$) is strictly forbidden in nature in such lattice sites. However, in an asymmetric environment, the ED is usually the most intense emission line since transition with $\Delta J = \pm 2$ are hypersensitive to slight deviation from inversion symmetry. This renders Eu^{3+} ion as one of the most preferred structural probe to understand the local symmetry, site occupancy *etc.*[23–27] There are many literatures available on optical properties of Eu^{3+} ion in LNO, which also reported that there are multiple sites for Eu^{3+}.[28,29]

Defect near to Eu^{3+} ion also creates asymmetric environment, which apparently affect the luminescence and lifetime properties. Thus in addition to Eu^{3+} ion's use as a structural probe it may gives significant information about the defect structures, which has influence on the ferroelectric properties. A more asymmetric environment surround the Eu^{3+} ions will also help in developing red phosphor with higher color purity due to highly intense ED line. However, a systematic study about the defect related emission in these matrixes and its effect on Eu^{3+} ion's characteristics emission, is highly missing in literature surveys.

As far as ferroelectric property is concerned, there is no single report available till date on the effect of Eu^{3+} ion doping on the ferroelectric properties of LNO. Therefore, it is of great importance now to conduct a systematic study on the ferroelectric and optical properties in Eu^{3+} doped LNO compound. For the first time, we are using Eu^{3+} ions as a structural probe to investigate the local distortion at the lattice sites in LNO matrix, especially in the first co-ordination shell to understand the impact on ferroelectric properties. Earlier, we have also carried out DFT based calculations in many matrices[30] in order to get information about the electronic states due to defect centers inside the band gap of the matrix and their correlation with the defect related emission. Using DFT based calculation, we have also shown how the dopant ion distribution among different lattice site changed the defect induced shallow and deep trap states and the following consequence on emission properties. Further, a significant information regarding the structural distortion upon Eu^{3+} doping at different lattice sites can also be achieved theoretically, which will be helpful to correlate the ferroelectric properties with the dopant ion's distribution. Therefore, a combined experimental and theoretical works on optical and ferroelectric properties of $LiNbO_3$ and Eu^{3+} doped $LiNbO_3$ (LNO:Eu^{3+}) will not only be helpful for designing new multifunctional materials for application in pizeo-photonic devices but also to advance the knowledge to control the multiple physical properties simultaneously in the desire range.

2. Experimental

2.1. Synthesis of $LiNbO_3$ and Eu^{3+} doped $LiNbO_3$

2.1.1. $LiNbO_3$ (LNO). $LiNbO_3$ has been prepared by solid state route. A homogeneous and equimolar mixture of Li_2CO_3 and Nb_2O_5 has been prepared and then pelletized to a cylindrical pellet. The pellet was heated upto 700 °C through several intermediate steps of heating, grinding and re-pelletization in high pure argon (oxygen and moisture free Ar) environment for 100 h. For purification of argon gas, the 99.999% pure argon gas was passed through several getters, uranium and BTS catalyst

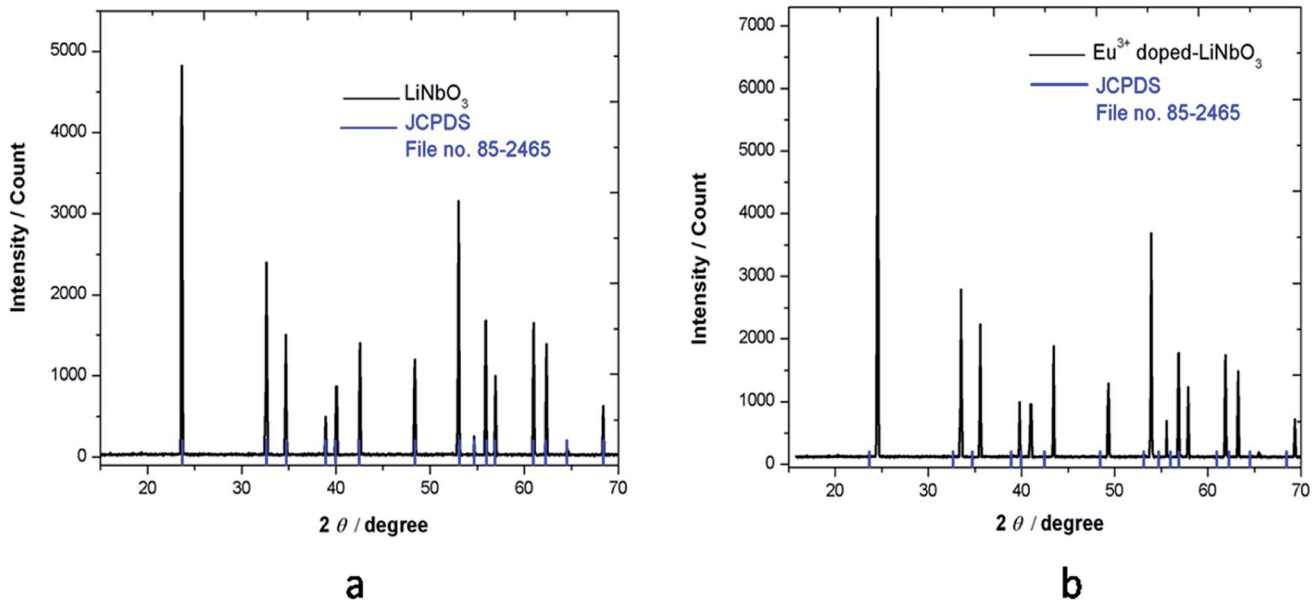

Fig. 1 XRD pattern of (a) $LiNbO_3$ and (b) Eu^{3+} doped $LiNbO_3$.

for oxygen removal; silica gel and magnesium perchlorate for moisture removal.

2.1.2. Eu^{3+} doped $LiNbO_3$ (Eu:LNO). 5.0 mol% Eu_2O_3 doped $LiNbO_3$ has been synthesized by heating of a homogeneous mixture of Eu_2O_3, Li_2CO_3 and Nb_2O_5 in stoichiometric amount in high pure argon atmosphere at 750 °C. The synthesis procedure is same as describe for $LiNbO_3$. The characterization of the sample has been carried out with X-ray diffraction technique.

2.2. Instrumentation

The instrumental details of all the techniques such as XRD, FTIR, and photoluminescence are given in ESI.†

3. Results and discussion

3.1. Phase purity by X-ray diffraction (XRD)

The prepared compounds were characterized by XRD technique. Fig. 1 shows the XRD pattern of $LiNbO_3$ and Eu^{3+} doped $LiNbO_3$, where all the peaks are well consistent with the reported in JCPDS file no. 85-2456, which indicates formation of pure compound for both un-doped and Eu^{3+} doped $LiNbO_3$ compounds.

3.2. Fourier-transform infrared (FTIR) spectroscopy study of LNO and Eu^{3+} doped LNO

The FTIR spectra were recorded using a diamond single reflection ATR probe Alpha Bruker-500 spectrometer. For LNO and Eu^{3+} doped LNO, the FTIR spectra have been shown in Fig. 2, and it shows that for both niobates, the absorption peaks exist in the range of 500–1000 cm^{-1}, which can be attributed the NbO_6 octahedron.[31]

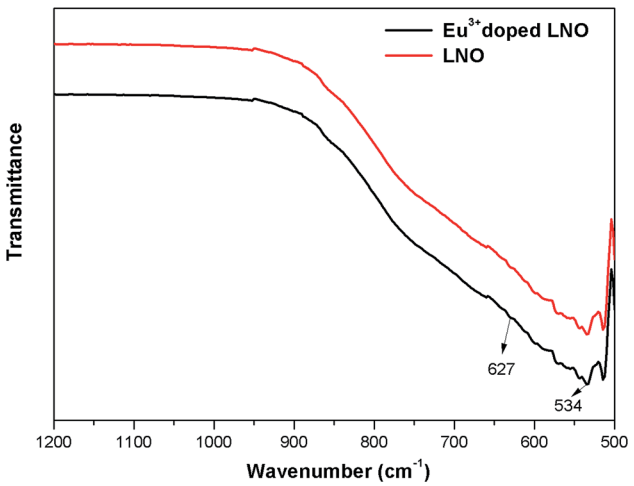

Fig. 2 FTIR spectra of LNO and Eu^{3+} doped LNO.

3.3. Photoluminescence study

3.3.1. Excitation, emission and lifetime studies of undoped LNO. Excitation and emission spectra of undoped LNO are presented in Fig. 3. It was found that the excitation spectrum consists of a broad host excitation band in 230–250 nm regions. The band is attributed to $O^{2-} \rightarrow Nb^{5+}$ charge transfer (CT) transition. Later on from our DFT calculation also, we have confirmed that the vacant 2p orbital of oxygen and d orbital of Nb are closely placed at around 5 eV (247 nm) and may involved with such kind of transitions. Fig. 3b showed the emission spectra of undoped LNO at 230 nm excitation wavelength, which showed two broad emission bands in the violet-blue and green regions. These multicolor emissions suggested that there

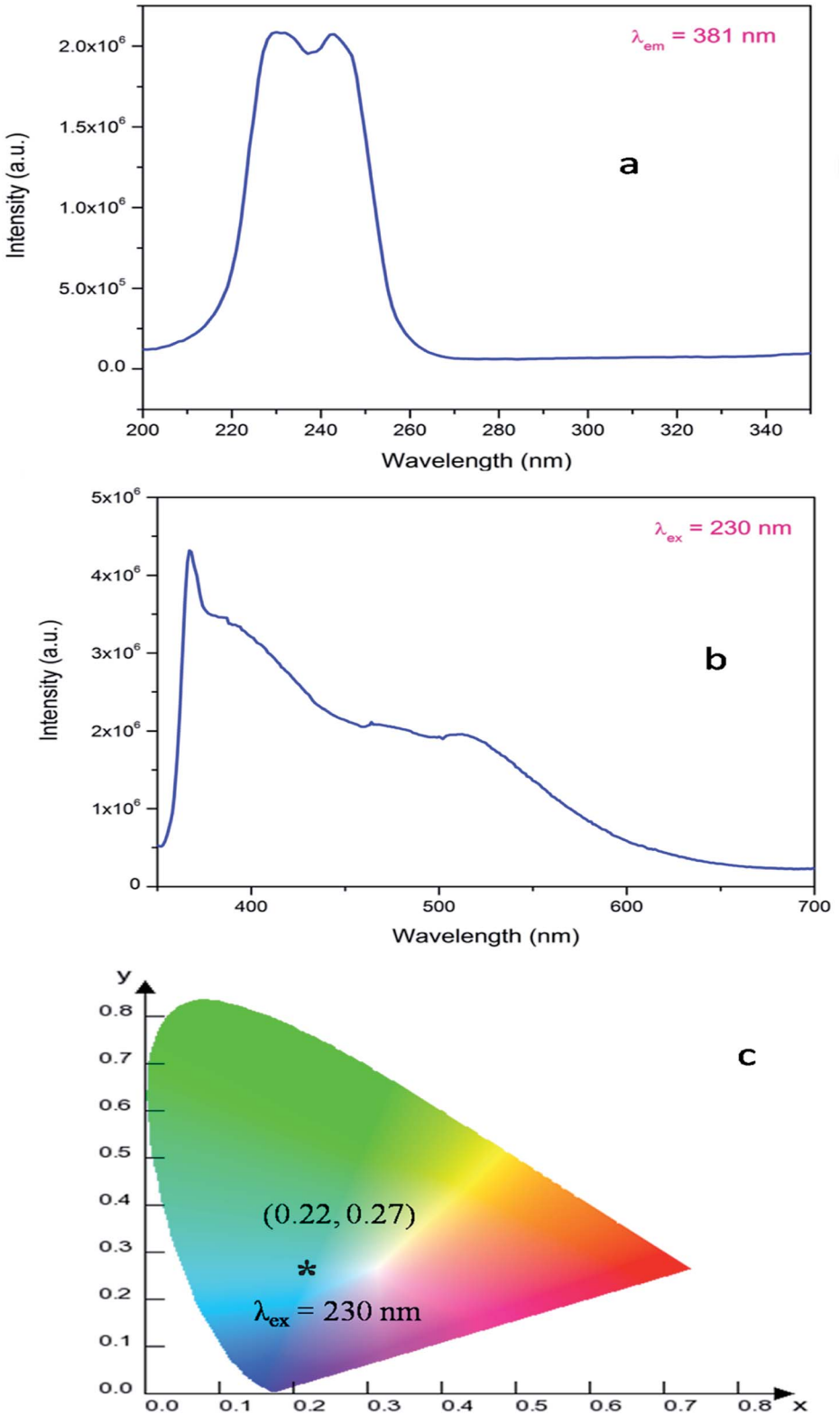

Fig. 3 Photoluminescence (a) excitation and (b) emission spectra of LNO recorded at room temperature and (c) the corresponding CIE color co-ordinates.

are different electronic states inside the band gap of the materials due to different defect centers. Each colour can be attributed to a specific electronic transition involving defect related trap state. From our DFT basd calculation (explained latter) we have seen that many defect centers such as neutral and differently charged oxygen vacancies *viz.* V_O^0, V_O^{1+}, V_O^{2+} *etc.* and

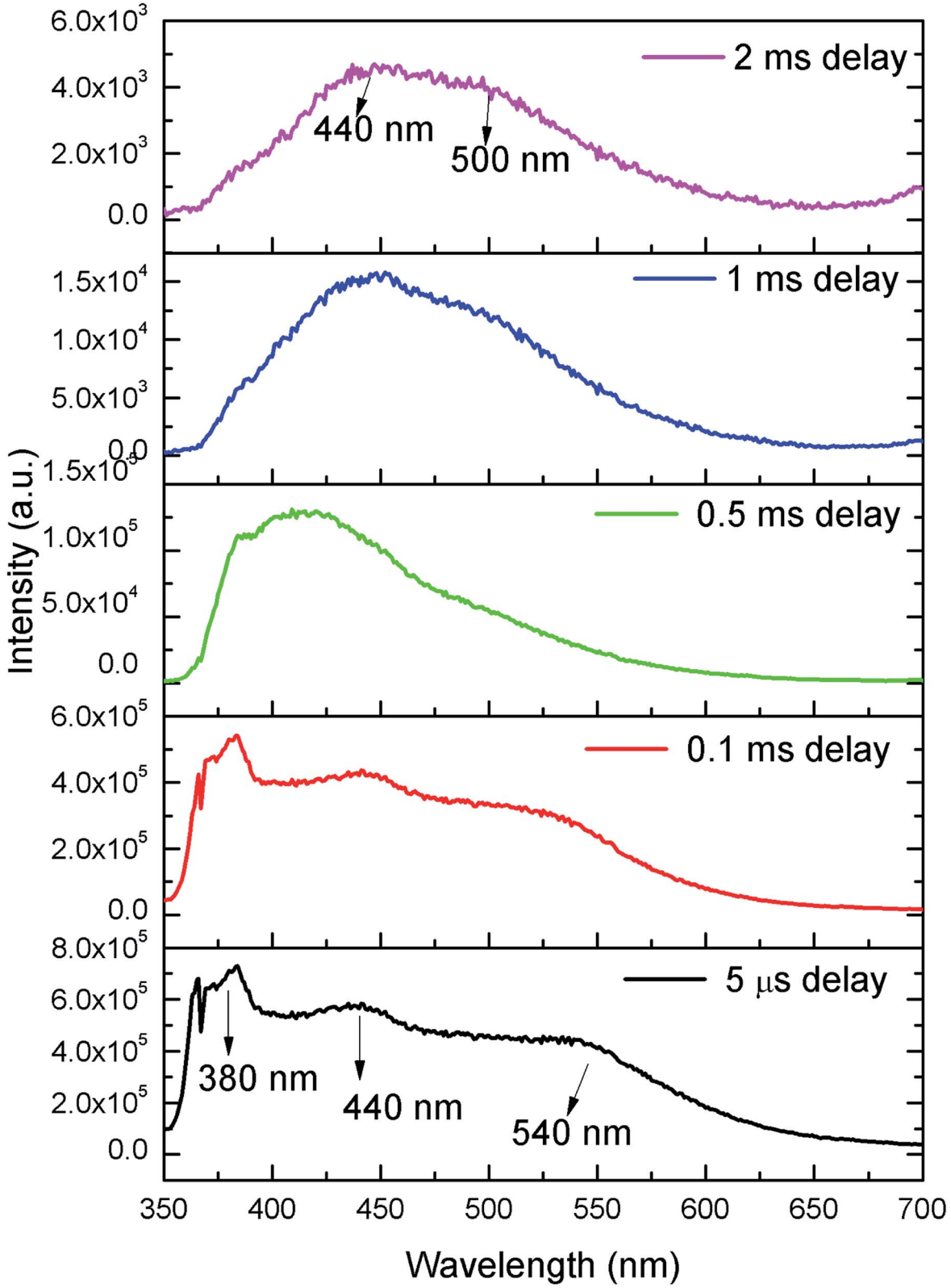

Fig. 4 TRES spectra of LNO at different delay time.

cationic vacancies such Li vacancies (V_{Li}^{1-}), creates different intermediate electronic states and must be responsible for such emission. The electronic state due to oxygen vacancies are close to that 2p orbital of oxygen and vacant d orbital of Nb. Hence after excitation at 230 nm from 2p orbital of oxygen to vacant d orbital of Nb, the electrons may jump to these states and

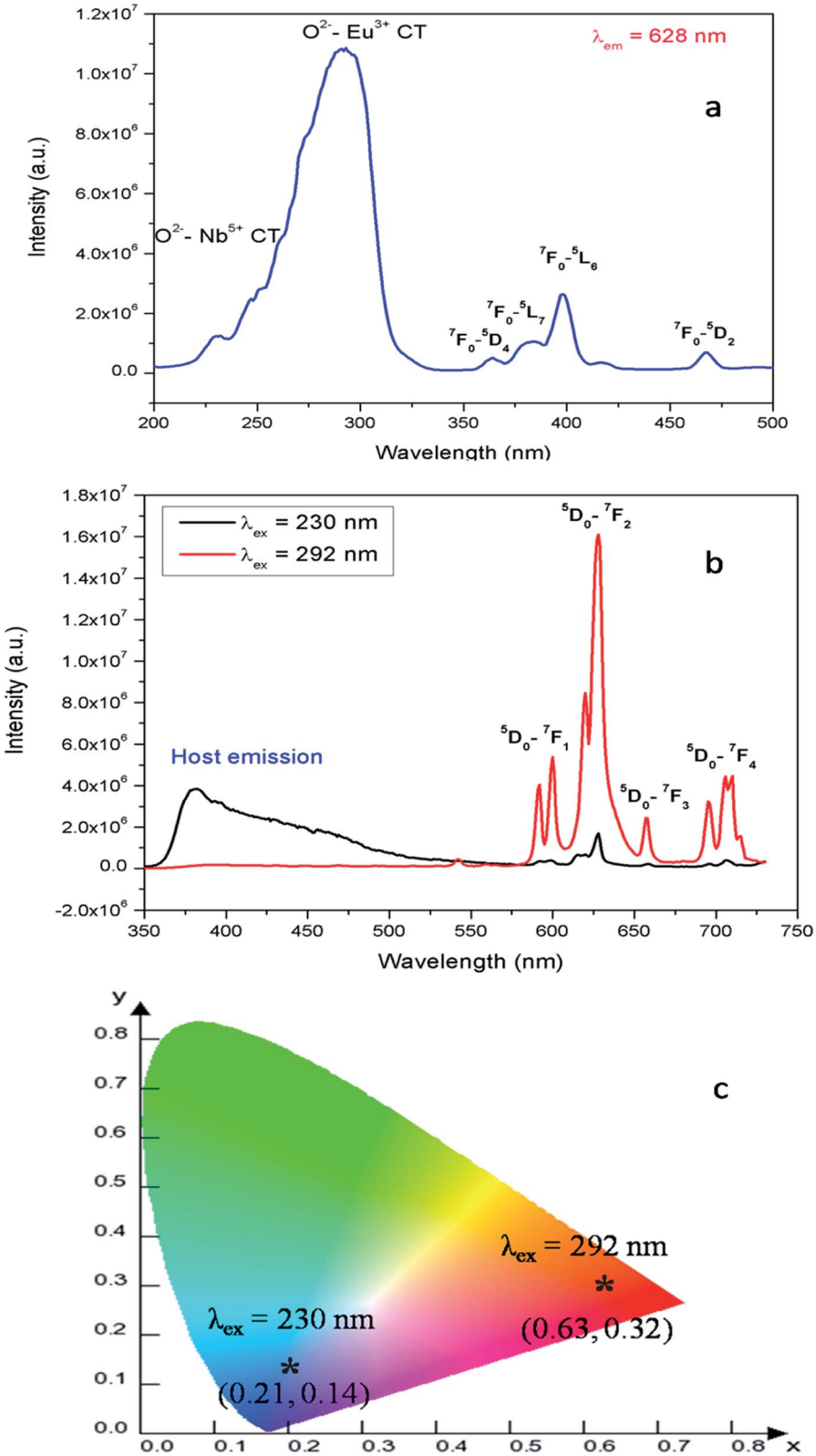

Fig. 5 (a) Photoluminescence excitation and (b) emission spectra of Eu:LNO recorded at room temperature and (c) the corresponding CIE color co-ordinates.

thereby gives rise to multicolor emission. Transitions between differently charged oxygen vacancies and between cationic vacancies are also found to be possible by theoretical studies with energy in the same wavelength regions as observed in the emission spectrum. In addition the charge transfer tarnsition in the NbO_6 octahedron also contributes to such emission band.

Fig. 3c, which represents the CIE color coordinate of the compound, indicates that the sample is bluish-green emitting material.

In order to identify various defect centres responsible for the host emission, PL lifetime measurements were carried out at 230 nm excitation and at different host emission band such as at 380 nm, 440 nm and 540 nm and the decay curves are presented by Fig. S1 provided in the ESI.† Similar to our earlier cases of several defect related luminescence material,[32] in LNO compound also, there is a possibility of getting multiple lifetime value at single emission wavelength due to overlap by other emission bands. However, we have considered only that lifetime value which has maximum contribution among all. The respective lifetime values are 113.16 μs for 380 nm color components, 618.40 μs for 440 nm color component and 130.83 μs for 540 nm color component. Further to confirm their existence in the broad emission spectra, we have carried out the Time Resolved Emission Spectra (TRES) analysis at different delay time. Fig. 4 represents the TRES spectra at different delay time. It is generally assumed that the excited species are completely decayed at a time which is equal or greater than three times of their respective lifetime value (3τ). Since most of the components have lifetime value more than 100 μs, the TRES spectra at 5 μs delay time is composed of all the color components. However, as we kept on increasing the delay time, there is a gradual change in intensity of the color components. The spectra at 380 nm and 540 nm region starts disappearing, since they are the short lived species and at a delay time of 1 ms, these two components are almost disappeared from the spectra, which is now composed by the 440 nm and 500 nm components. The 500 nm component was not visible in the emission spectra, however the TRES study showed that there is a color emitting component at 500 nm region which is having higher lifetime value than the 440 nm component that is 1908.30 μs.

3.3.2. Excitation, emission and lifetime studies of Eu:LNO. Fig. 5a represents the photoluminescence excitation (PLE) spectrum of Eu:LNO at $\lambda_{em} = 628$ nm, which is attributed to the $^5D_0$–$^7F_2$ transition of Eu^{3+} ion. The PLE spectrum is composed of an intense broad peak in the 220–330 nm wavelength range along with some weak sharp features in the 330–500 nm range. The intense broad band in the 220–330 nm range also consist of three features; the 230–250 nm band is host absorption band that is $O^{2-} \rightarrow Nb^{5+}$ charge transfer (CT) transition, while the highly intense peak around 292 nm must be due to the $O^{2-} \rightarrow Eu^{3+}$ CT transitions.[31] Later on from our DFT calculation, we have found that the vacant 2p orbital of Oxygen and the d orbital of Eu^{3+} ions are closely placed at around 4 eV in the conduction band and may be responsible for this transition. The peaks in the 330–500 nm range are due to f–f transition of Eu^{3+} ions[33] wherein the $^7F_0 \rightarrow {}^5L_6$ (396 nm) is the most intense one.

Fig. 5b represents the emission spectrum of Eu:LNO$^+$ upon excitation with both the host absorption band ($\lambda_{max} = 230$ nm) and with the CT band of Eu^{3+} ($\lambda_{max} = 292$ nm). It can be seen from the respective figures that upon excitation with 230 nm the host emission band is the most intense one. On the other hand upon excitation at 292 nm the emission spectrum exhibits

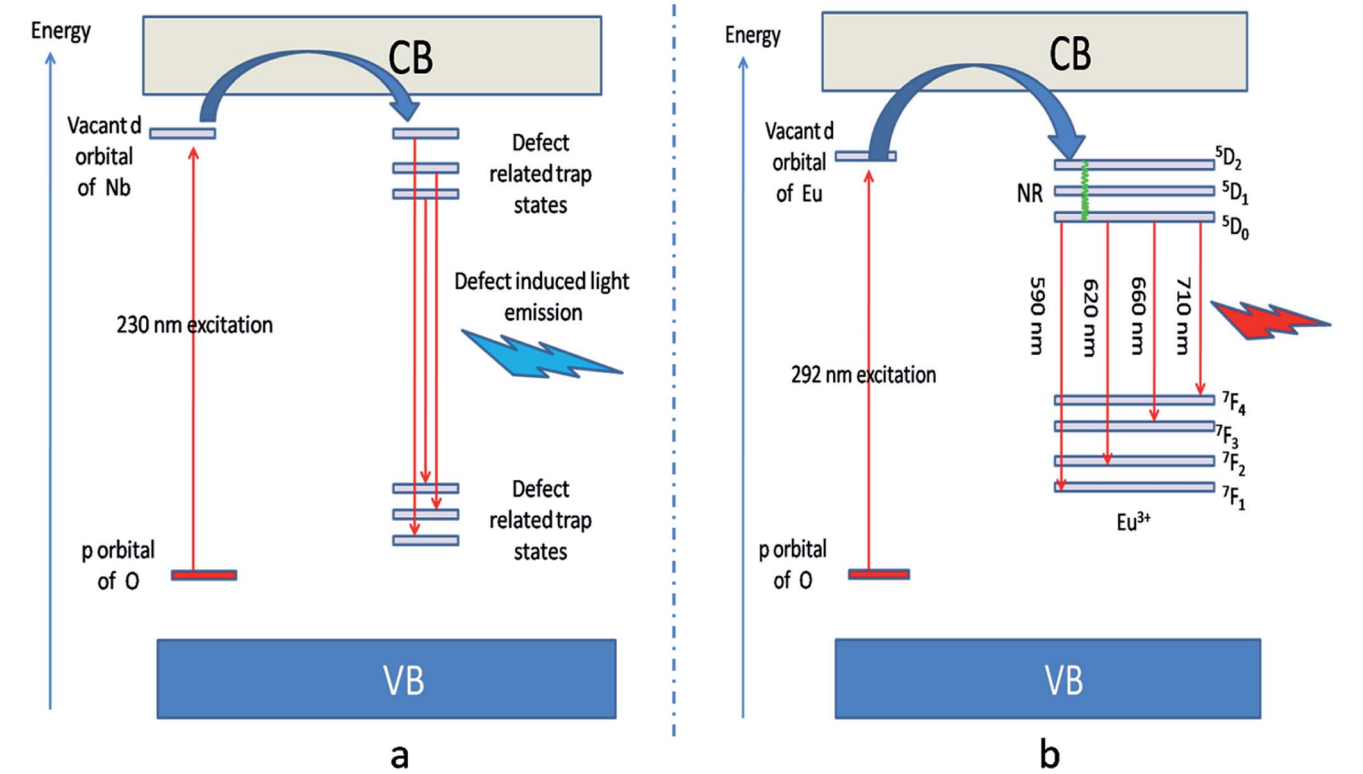

Fig. 6 (a) defect induced host emission at 230 nm excitations and (b) Eu^{3+} ions emission at 292 nm excitation. The defect related trap states are observed from DFT calculation and they are due to various oxygen, Li and Nb vacancies. A pictorial summary of such defect related energy states inside the band gap has been given in Fig. S2 in ESI.†

intense characteristics features of Eu^{3+} ion involving transition from $^5D_0$ to ^7F_J, $J = 0$–4. In this case, the host emission bands are almost disappeared. The color coordinates, as represented by the asterisk "*", are given in the CIE chromaticity diagram in Fig. 5c, which shows that upon changing the excitation from 230 nm to 292 nm, the Eu:LNO compound changes its emission from bluish to red. This is a very interesting observation due to fact that the same compound can be used both as blue light emitting as well as red light emitting phosphor material by choosing different excitation source *i.e.* either with a short-wave UV source or by a long wave UV source. This can be explained on the basis of the respective CT excitation bands of host ($O^{2-} \rightarrow Nb^{5+}$) and Eu^{3+} ion ($O^{2-} \rightarrow Eu^{3+}$). When we are exciting with the 230 nm, which is CT from $O^{2-} \rightarrow Nb^{5+}$, the compound is showing intense bluish host emission but at 292 nm excitation, which is due to CT from $O^{2-} \rightarrow Eu^{3+}$, the compound will definitely show the red emission of Eu^{3+} ion. From the emission spectra of Eu^{3+} ions, it can also be seen that $^5D_0 \rightarrow {}^7F_2$ electrical dipole transition (ED) around 628 nm is more intense than the $^5D_0 \rightarrow {}^7F_1$ magnetic dipole (MD) transition around 595 nm. This indicates that most of the Eu^{3+} ions in LNO are occupying an asymmetric site.[31,33] Let us propose a possible band structure model by Fig. 6, which pictorially explains all these observation. All these electronic states are later explained in out DFT calculation part. From Fig. 6a, it can be seen that the electrons are being excited from filed p orbital of O to vacant d orbital of Nb^{5+} at 230 nm wavelength. Now since this state is very close to many defect related energy states or the conduction band, the electrons can transfer to these states *via* the conduction band and thereby gives rise to various defect related emissions. In Fig. 6b, the electrons from p orbital of O to vacant d orbital of Eu^{3+} ion are excited at 292 nm wavelength and gives rise to its characteristics emissions. A detail study of these energy states are given latter in the theoretical part.

In order to understand the local environment and site occupancy of Eu^{3+} ions in LNO, PL lifetime experiments were carried out at 395 nm excitation and 628 nm emission wavelengths. The decay curve was best fitted with the bi-exponential eqn (1) as shown in Fig. 7.

$$I(t) = A_1 \exp\left(-\frac{t}{\tau_1}\right) + A_2 \exp\left(-\frac{t}{\tau_2}\right) \quad (1)$$

where $I(t)$ = intensity, τ_1 and τ_2 are the respective lifetime values of different components, while A_1 and A_2 are relative weights.

To calculate the percentage of a specific lifetime component the following formula can be used

$$\%\ \text{of species}\ n = \left[\frac{(A_n \times \tau_n)}{\sum_{n=1,2} A_n \times \tau_n}\right] \times 100 \quad (2)$$

The two different lifetimes obtained from the decay curve are $\tau_1 = 643.16$ μs and $\tau_2 = 706.99$ μs with the relative percentage of 23% and 77% respectively. The average lifetimes (τ_{ave}) is calculated using the eqn (3).

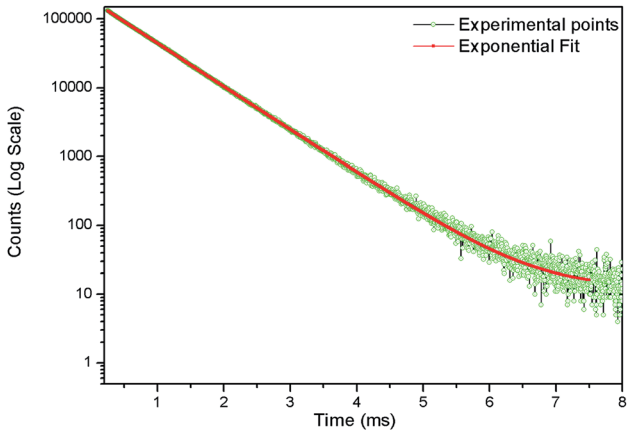

Fig. 7 Photoluminescence decay curve of LNO:Eu^{3+} at $\lambda_{ex} = 395$ nm with (a) $\lambda_{em} = 628$ nm.

$$\tau_{ave} = \frac{(A_1\tau_1^2 + A_2\tau_2^2)}{(A_1\tau_1 + A_2\tau_2)} \quad (3)$$

where A_1 and A_2 are residual weightage as obtained from eqn (3). The average lifetime obtained here is $\tau_{ave} = 701.17$ μs.

The observation of two lifetime values suggests that Eu^{3+} ions must be placed in two different lattice environments. From ionic radii consideration, 6 co-ordinates Eu^{3+} is larger (ionic radii = 0.94 Å) in size compared to both 6 co-ordinate Nb^{5+} (ionic radii = 0.64 Å) and 6 co-ordinate Li^{1+} (ionic radii = 0.76 Å). If Eu^{3+} ions go to any of these two lattice sites then there will a charge difference of 2, either negative or positive and to compensate this charge imbalance there will be creation either positively charged oxygen vacancies (formation of a V_O^{2+}, if Eu^{3+} ion goes to Nb^{5+} site) or negative charged cationic vacancies (formation of $2V_{Li}^{1-}$, if Eu^{3+} ion goes Li^{1+} site). From our theoretical calculation we have observed that formation energy of V_O^{2+} is less compared to that of V_{Li}^{1-}. Further there should be creation of two Li-vacancies if Eu^{3+} goes to Li^+ site. Thus Eu^{3+} ion has more preference to go to the Nb^{5+} site. Therefore, the $\tau_2 = 706.99$ μs component with a relative percentage of 77% might be due to Eu^{3+} ions at Nb^{5+} site while $\tau_1 = 643.16$ μs with a relative percentage of 23% might be due to Eu^{3+} ions at Li^+ site. We have also observed from theoretical calculation that a Eu^{3+} ion replacing Nb^{5+} site is energetically more favorable.

3.3.3. Stark splitting patterns in Eu:LNO. As reported earlier that point symmetry of LNO trigonal structure is C_{6v}.[34] However, when Eu^{3+} is doped in LNO host it is very much expected that because of the charge difference there will be formation of defects such as V_O^{2+} and V_{Li}^{1-}. In addition size mismatch will also result in lattice strain. The cumulative effect will result in a low symmetry and distorted local environment surround the Eu^{3+} ions. This is also supported by the high intense ED transition of Eu^{3+} as observed for the Eu^{3+} doped LNO compound. Now similar to earlier reports, we have also investigated the stark splitting patterns of the characteristics emission lines of Eu^{3+} ion in order to understand the point symmetry around Eu^{3+}.[26] Generally in a ligand environment, the $(2J + 1)$-degenerate J-levels of Eu^{3+} ion splits into so-called Stark sub-levels and their number depends on the local site symmetry

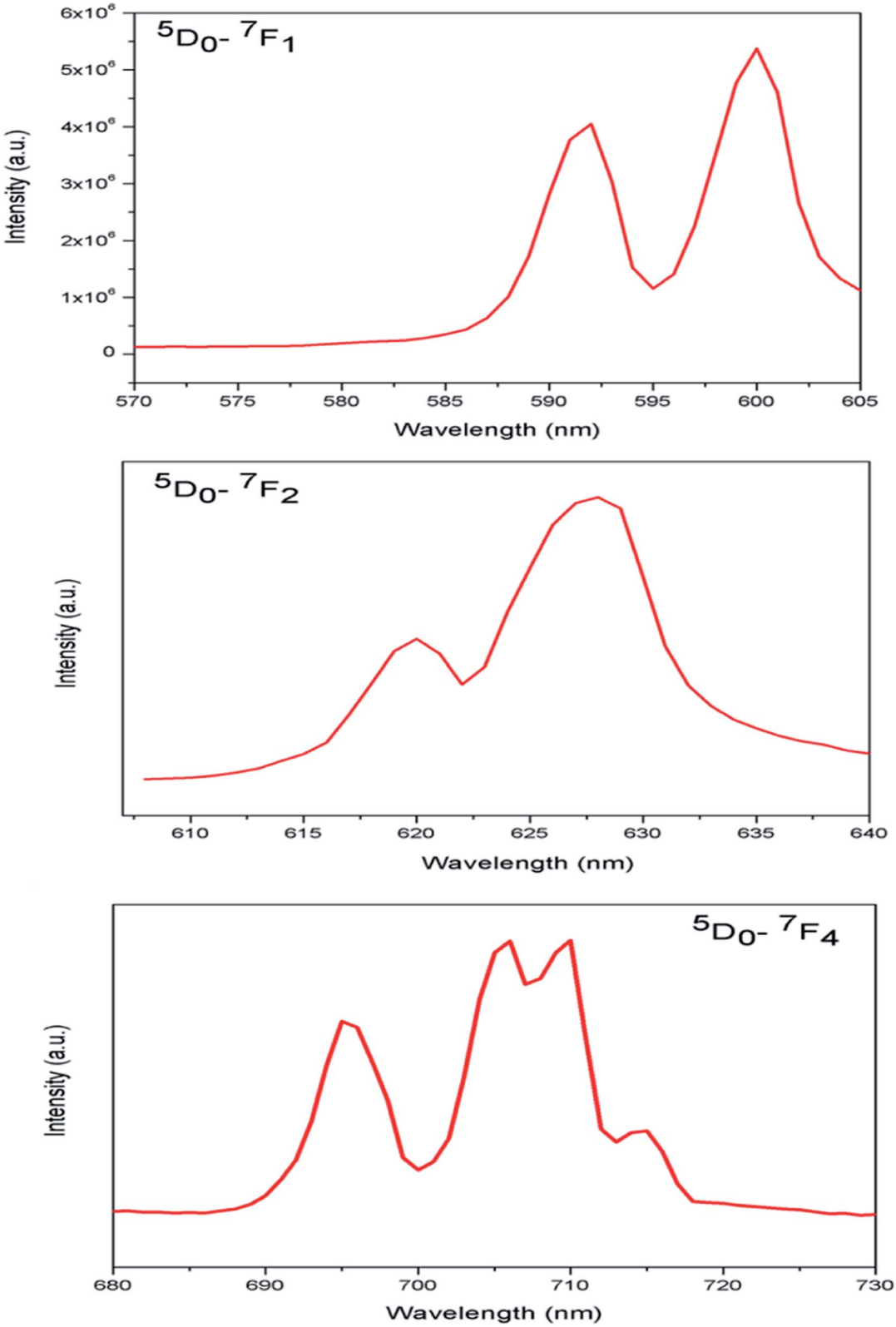

Fig. 8 Stark splitting pattern of the characteristics emission lines of Eu^{3+} ion in LNO.

of the metal ion. It is known that the electronic transitions from $^5D_0$ to ground levels with $J = 0$ or odd J ($J = 3, 5$) are forbidden (both ED and MD) in nature and some weak transitions to these levels are only possible when there is a CF induced J-mixing effect[35]. Again as per ED selection rule, the $^5D_0 \rightarrow {}^7F_0$ transition is only allowed in compounds which have site symmetries C_s, C_1, C_2, C_3, C_4, C_6, C_{2v}, C_{3v}, C_{4v}, and C_{6v} respectively.[36]

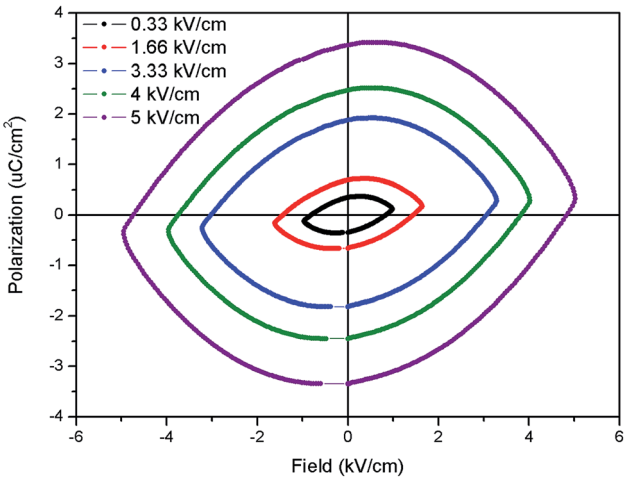

Fig. 9 Ferroelectric (*P–E*) hysteresis loops of the Eu:LNO at room temperature at different electrical field.

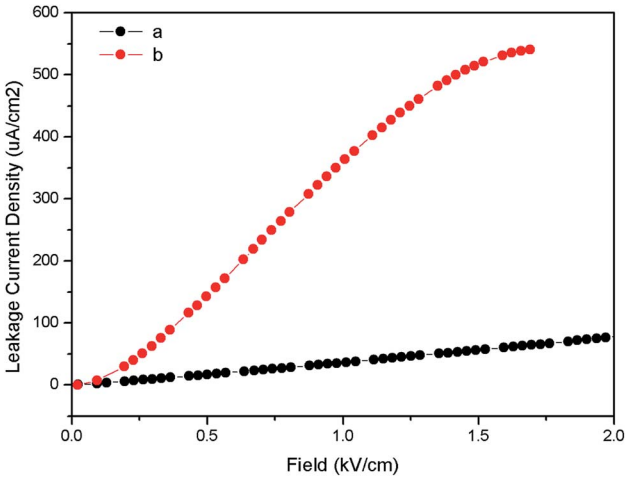

Fig. 11 Leakage current density *vs.* field (a) LNO and (b) Eu:LNO.

In present case the $^5D_0 \rightarrow {}^7F_0$ transition is absent and hence the site symmetry should not be among those mentioned above.

In case of Eu:LNO, the substitutions of Li^{3+} with Eu^{3+} will not result significant lattice distortion because of size difference is less. From stark splitting pattern shown in Fig. 8, two peaks for $^5D_0 \rightarrow {}^7F_1$ MD transition, three peaks for $^5D_0 \rightarrow {}^7F_2$ ED transition and four peaks for $^5D_0 \rightarrow {}^7F_4$ transition of Eu^{3+} ion were resolved for Eu:LNO. Therefore from the branching rules for various point groups;[37,38] we can say that in Eu:LNO the actual site symmetry of Eu^{3+} is D_3. Thus it can be conclude that upon Eu^{3+} doping the structure becomes less symmetric due to distortion.

3.4. Electrical properties

The ferroelectric (*P–E*) hysteresis loops of the Eu:LNO at room temperature and at different electrical field is shown in Fig. 9. It is observed that the polarisation is maximum at 5 kV cm^{-1}. It is very crucial to characterize the ferroelectric behaviour from *P–E* loop and earlier reports showed that the compounds which shows saturation in polarization and have concave region in *P–E* plot are true ferroelectric in nature.[39] The present compound also showed saturation polarization and concave region, which indicates the presence of intrinsic ferroelectricity.

Fig. 10 represents the ferroelectric (*P–E*) hysteresis loops for undoped and Eu^{3+} doped samples at a field 5 kV cm^{-1}. The respective remnant polarization of Eu:LNO and LNO samples are Pr = 3.3652 μC cm^{-2} and Pr = 0.30 μC cm^{-2} respectively. While the energy loss are 13 864.5 μJ cm^{-2} for Eu:LNO and 1311.82 μJ cm^{-2} for LNO. Figure represent the leakage current density *vs.* field plot for Eu:LNO and LNO, from which it can be seen that the leakage current is more at any point of field for Eu:LNO compare to LNO.

A detail description of crystal structure of LNO shows that it belongs to a *R3c* space group.[40,41] The oxide ions are arranged in nearly hexagonal close-packed planar sheets and the stacking sequence of cations in these octahedral sites is: Nb, Li, vacancy, Nb, Li, vacancy… and so on or LiO_6, NbO_6 and VO_6…, where V stands for vacancy. It is worth to note here that one third of the octahedral interstices are filled by lithium atoms, another one-third filled by niobium atoms, and the remaining one-third is vacant. The Li and Nb ions are placed significantly off-center from the centrosymmetric positions along the polar axis and

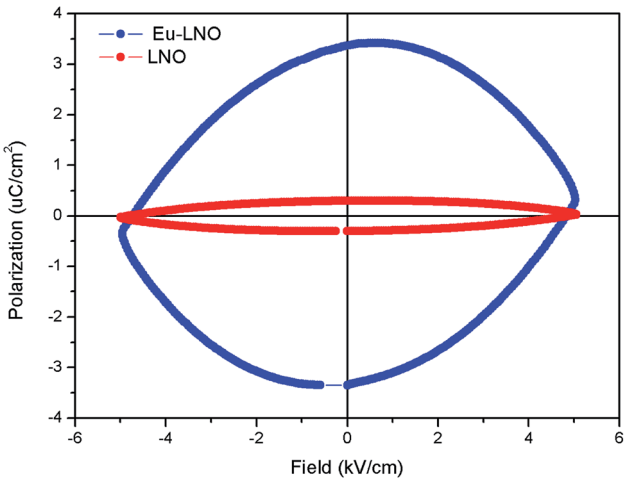

Fig. 10 Ferroelectric (*P–E*) hysteresis loops for undoped (LNO) and Eu^{3+} doped samples (Eu–LNO) at a field 5 kV cm^{-1}.

Table 1 Our DFT-GGA calculated lattice constants and atomic positions of perfect lithium niobate are compared with previous experiment and DFT calculated results[a]

	a	*c*	*z*	*u*	*v*	*w*
DFT-GGA (this study)	5.197	14.017	0.0329	0.00881	0.0388	0.0191
Experiment[43]	5.151	13.876	0.0329	0.00947	0.0383	0.0192
DFT-LDA[42]	5.086	13.723	0.0350	0.01497	0.0247	0.0186
DFT-GGA[44]	5.067	13.721	0.0337	0.01250	0.0302	0.0183
DFT-GGA[45]	5.161	13.901	0.0339	0.01205	0.0278	0.0191

[a] For $LiNbO_3$, in hexagonal coordinate, *z*, *u*, *v* and *w* were defined (0; 0; 1/4 + *z*) for Li1, (0, 0, 0) for Nb1, and (−1/3 − *u*; −1/3 + *v*; 7/12 − *w*) for O1 (ref. 45).

this result in spontaneous polarization. Therefore, any distortion at Li or Nb-site in the matrix will affect the position of these ions and change the spontaneous polarization. Thus, the increase in polarization of LNO matrix upon doping with Eu^{3+} ion can be correlated with relatively more off-center position of these Nb and Li ions due to substitution of Eu^{3+} ion. It is quite obvious that 6-coordinated Eu^{3+} ion has bigger ionic radii than same coordinated Nb^{5+} and Li^{+} ion. Therefore, there will be high degree of distortion in the matrix due to substitution of smaller ion by bigger ion. Further, the charge imbalance will cause addition distortion and may results in several defect centers. This is also reflected in the leakage current density plot in Fig. 11 which showed that the leakage current is more when Eu^{3+} is doped into the LNO matrix. As stated earlier that Eu^{3+} substitution at Nb-site of LNO results in defects, which may increase the ionic conductivity. This increased conductivity causes more leakage in current. The enhancement of polarization also indicates that the dopant ion Eu^{3+} is going to the lattice site and not to the vacant interstices site, otherwise a decrease in polarization would have been observed since it would restrict the displacement of Li or Nb to other side of oxygen triangle.

3.5. Electronic structure and band gap energy of LNO and the possible explanation for photoluminescence and electrical observations

The DFT calculation mythologies are given in the ESI.† Generally, at room temperature the ground state of LNO is

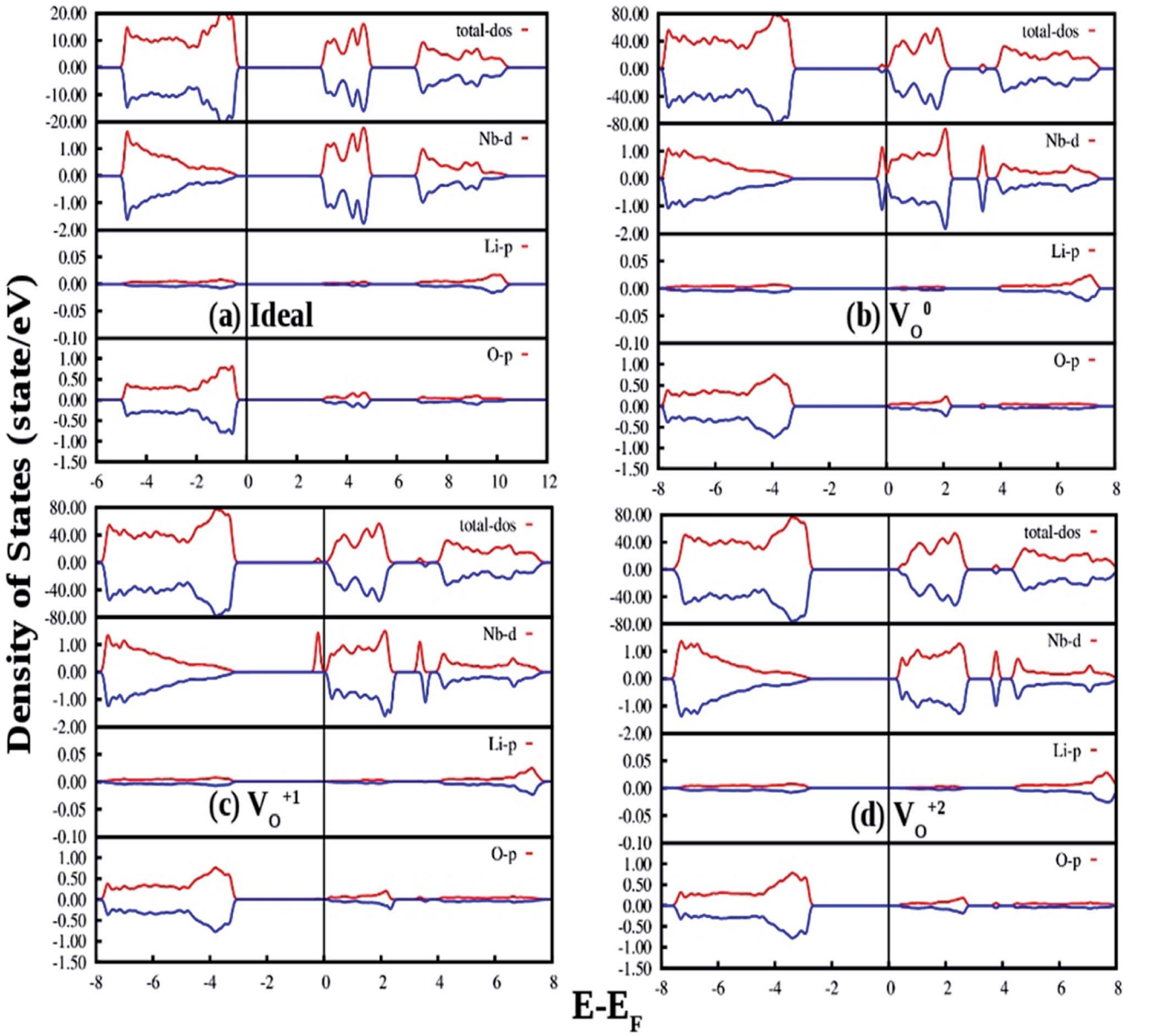

Fig. 12 Total and species projected DOS for (a) ideal LNO and with (b) neutral oxygen vacancy (V_O^0 or F^0), (c) singly charges oxygen vacancy (V_O^{1+}, F^+) and (d) doubly charged oxygen vacancy (V_O^{2+}, F^{2+}) calculated in a 120 atom supercell using DFT-GGA. The Fermi energies are represented by vertical lines at zero energy. The DOS for spin-up and spin-down states are represented by red and blue color respectively.

ferroelectric with space group $R3c$ while at high temperature (≥1480 K), the stable phase is high-symmetric paraelectric phase with space group $R\bar{3}c$. In ferroelectric ($R3c$) phase, the Li and Nb atoms are located at 6a Wyckoff position (in hexagonal axes) with internal parameter z_{Nb}, and O atoms are located at 18b Wyckoff position with parameters u, v, and w. We have followed the notation of ref. 42, the DFT-GGA calculated unit cell parameters are: $a = 5.197$ Å, $c = 14.017$ Å, $z_{Nb} = 0.0329$, $u = 0.00881$, $v = 0.0388$, and $w = 0.0191$. The reported unit cell parameters by experiment[43] are $a = 5.151$ Å, $c = 13.876$ Å, $z_{Nb} = 0.0329$, $u = 0.00947$, $v = 0.0383$, and $w = 0.0192$ and the deviation is less than 3% for the ferroelectric phase. Our GGA-PBE calculated results (given in Table 1) are also in well agreement with the GGA-PW91 results reported by Veithen and Ghosez.[44]

The density of states (DOSs) of ideal ferroelectric phase of LNO is plotted in Fig. 12(a). The band between −18 eV and −15 eV is mainly contributed by O 2p state. The upper valence-band (VB) lying in the range 0 and −5 eV can be divided into two different regions. In the low-energy region it can be observed that the O 2p states are strongly hybridize with Nb 4d states while the high-energy region was found to be predominately contributed by the O 2p states. The conduction band (CB) above the Fermi level of LNO is found to be dominated by Li 2s/2p states and O 2p states. This suggests that there is a possibility of charge transfer transition from 2p orbital of oxygen to 4d orbital of Nb as observed in our photoluminescence excitation spectra of LNO represented by Fig. 3a. The electronic band-gap in ferroelectric phase is 3.24 eV, which is in well agreement with reported result of 3.48 eV calculated by DFT-GGA.[45]

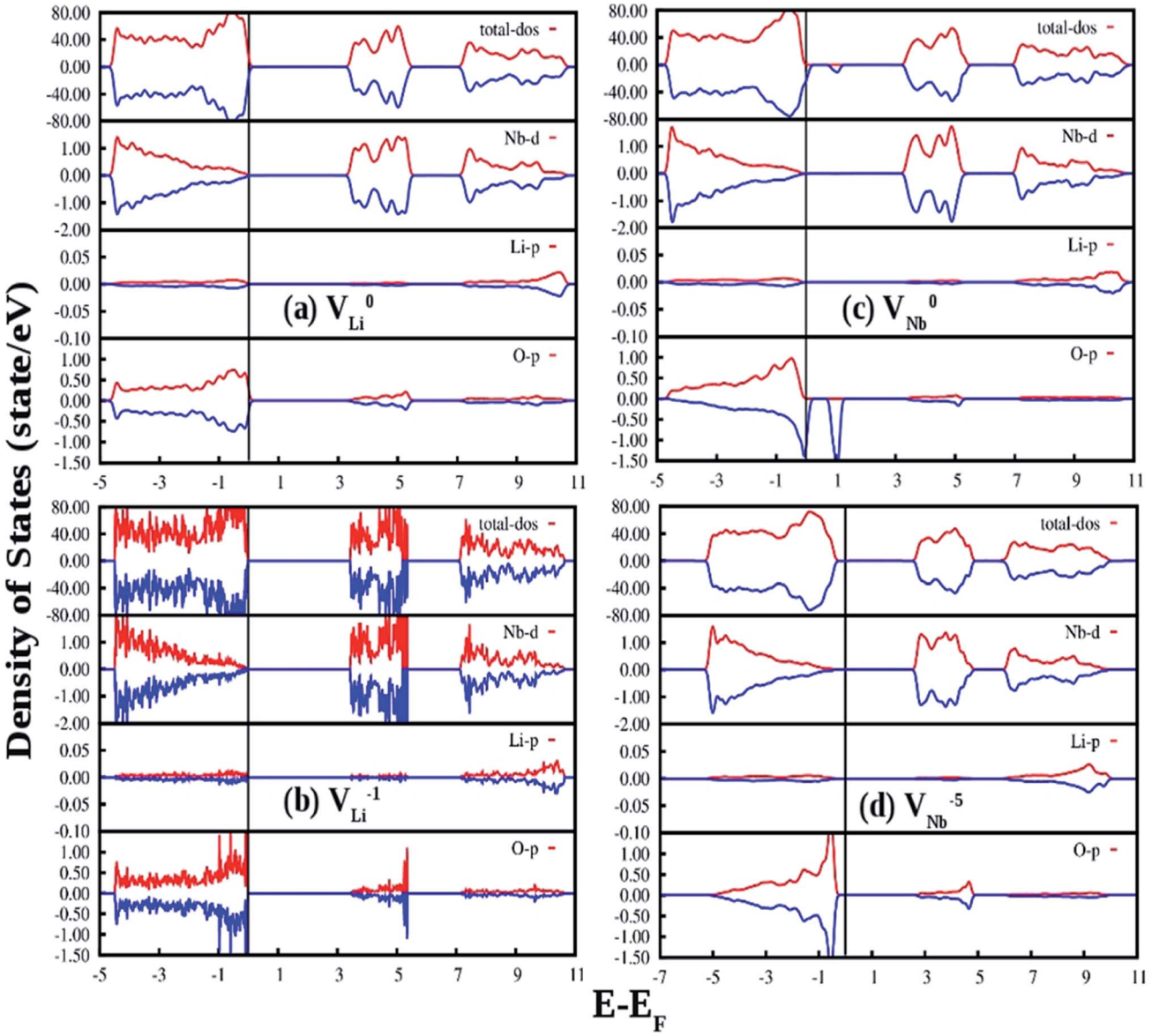

Fig. 13 Total and species projected DOS for LNO with (a) neutral Li oxygen vacancy (V_{Li}^{0}), (b) −1 charge Li vacancy (V_{Li}^{1-}), (c) neutral Nb vacancy (V_{Nb}^{0}) and (d) −5 charge Nb vacancy (V_{Nb}^{5-}) calculated in a 120 atom supercell using DFT-GGA. The Fermi energies are represented by vertical lines at zero energy. The DOS for spin-up and spin-down states are represented by red and blue color respectively.

Fig. 12(b) shows our GGA-PBE calculated DOS of LNO with a single neutral oxygen vacancy (V_O^0). Overall DOS features are similar to the ideal LNO case but an impurity states appear just below the CB minimum. The impurity states contribute both in majority and minority spin-component. It can be seen that the impurity state is mainly contributed by the Nb d state, which results in reduction of the electronic band-gap to 2.8 eV. Fig. 12(c) represents the GGA-PBE calculated DOS of LNO with a single +1 charge oxygen vacancy (V_O^{1+}). Overall DOS features are similar to the ideal LNO case but an impurity states appear just below the CB minimum. This impurity state contributes only in majority spin-component and contributed by the Nb d states. As a result the electronic band-gap is reduced to 2.7 eV. Fig. 12(d) represents the GGA-PBE calculated DOS of LNO with a single +2 charge oxygen vacancy (V_O^{2+}). Overall DOS features are similar to the ideal LNO case and no impurity states appear in the electronic band-gap region. The electronic band-gap was calculated to be 3.0 eV. In ideal LNO case Fermi energy is situated just above the VB maxima and in oxygen defect case (V_O^0, V_O^{1+}, V_O^{2+}) it is situated just below the CB minima. Therefore these impurity states inside the band gap in cases of V_O^{1+} and V_O^0 may be responsible for many electronic transition and gives rise to multicolor emission presented in Fig. 3a and 4. A pictorial representation of the defect related impurity electronic states is presented by Fig. S2 in the ESI.†

Fig. 13(a) and (b) represent the GGA-PBE calculated DOS of LNO with a single neutral and −1 charge Li vacancy (V_{Li}^0 and V_{Li}^{1-}), respectively. Overall DOS features are similar to the ideal LNO case and a few states are extended just above the Fermi energy with no other impurity states in the electronic band-gap region. The band-gap in V_{Li}^0 and V_{Li}^{1-} case is 3.17 and 3.30 eV, respectively, and Fermi energy is situated just above the VB maxima. Fig. 13(c) and (d) represents the GGA-PBE calculated DOS of LNO with a single neutral and −5 charge Nb vacancy (V_{Nb}^0 and V_{Nb}^{5-}), respectively. The DOS feature of V_{Nb}^0 is severely distorted in minority spin component as the minority spin component of 2p states of O atom situated in the 1st nearest neighbor to the Nb atom is modified. Moreover, an impurity state appear 0.5 eV ahead of VB maxima in minority spin component. In this case the degeneracy between spin-components are lifted. The electronic band gap in V_{Nb}^0 case is 3.0 eV. The DOS due to V_{Nb}^{5-} is almost resemblance the DOS of ideal LNO and the electronic band-gap is 2.57 eV. Therefore, the Li vacancies have least effect on the DOS and Nb vacancies distort the DOS appreciably. From electronic transition point of view, only V_{Nb}^0 gives rise to an additional electronic state inside the band gap and may take part in the host emission band.

Fig. 14(a) shows our GGA-PBE calculated DOS of LNO with an antisite defect where position of one Li and Nb atom is exchanged in the 120 atom supercell. Overall DOS features are similar to the ideal LNO case and no impurity states appear in the electronic band-gap region. The Fermi energy has shifted to the bottom of the CB minima in this case. But the Nb d-states present in the CB region is modified and the electronic band-gap is 2.30 eV in this case. Thus antisite defects have no role in the host emission. Fig. 14(b) and (c) shows our GGA-PBE calculated DOS of LNO with a Eu atom doping in Li and Nb site, respectively, in the 120 atom supercell. In our calculation one Eu atom is placed in Li and Nb site by removing 1 Li and 1 Nb atom out of 24 atoms. Due to Eu doping in Li site the Fermi energy has shifted to the bottom of the CB minima. An impurity state appears just below the CB minima in the minority spin component. The impurity state is composed of Eu d-states. On the contrary, a impurity state appears just above the VB maxima in both minority and majority spin component in case of Eu doping Nb site and the impurity state is contributed by the Eu f

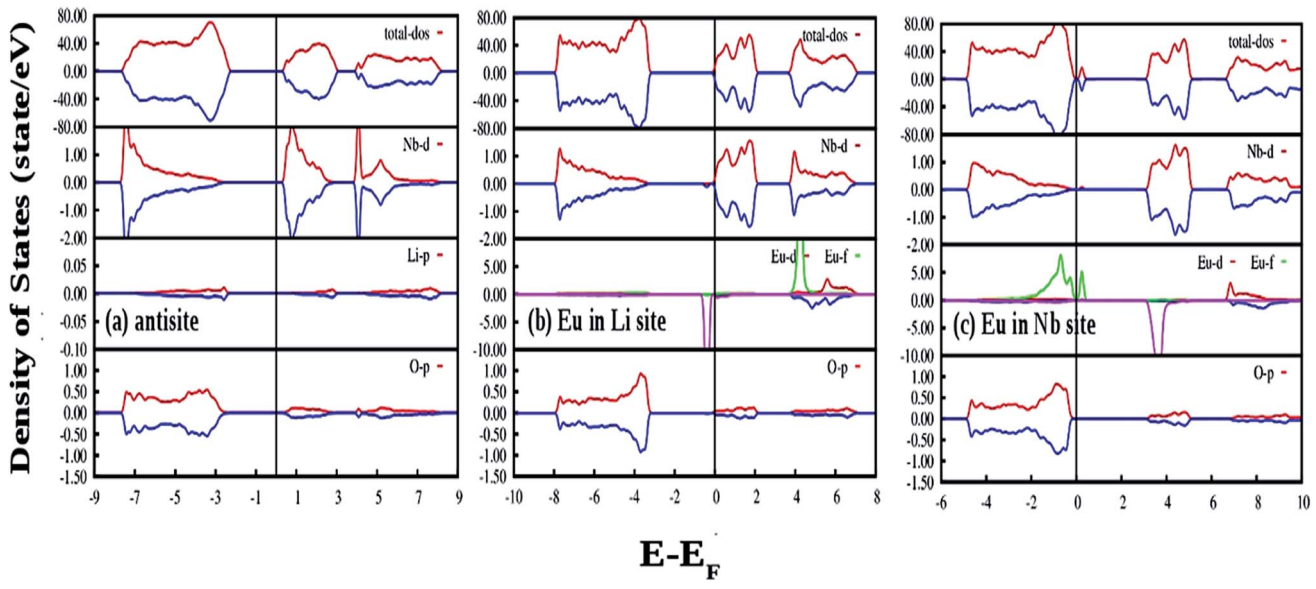

Fig. 14 Total and species projected DOS for LNO with (a) antisite defect and (b and c) shows the DOS of LNO with Eu doping in Li and Nb site, respectively, calculated in a 120 atom supercell using DFT-GGA. The Fermi energies are represented by vertical lines at zero energy. The DOS for spin-up and spin-down states are represented by red and blue color respectively.

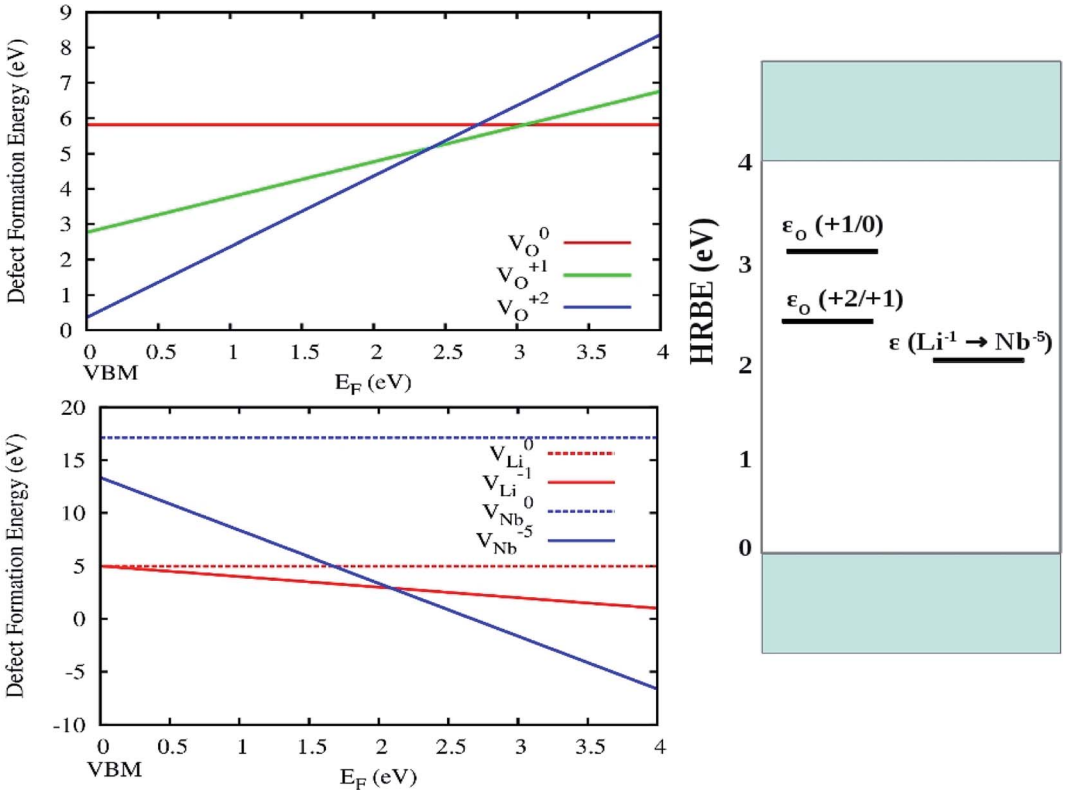

Fig. 15 DFT-GGA calculated defect formation energy (E_f) as a function of Fermi level (E_F) for charged defect states (q). Three charge-state transition levels are shown and they are a deep donor level ε (+2/+1) at 2.4 eV (516 nm), a deep donor level ε (+1/0) at 3.0 eV (413 nm) and another level ε (Li^{1-}/Nb^{5-}) at 2.2 eV (563 nm). These charge-state transition levels with respect to the host referred binding energies (HRBE) are shown in a conventional diagram on the right hand side.

states. The Fermi energy is situated just above the VB maxima for the Eu doping in Nb site. The electronic band-gaps are 2.25 and 2.40 eV for the Eu doping in Li and Nb site, respectively. From the DOS in cases of Eu placed at Nb site, it can be seen in the conduction band the vacant impurity states due to p orbital of oxygen and d and f orbital of Eu are closely placed around 4 eV. Thus there is probability that the excited electron from the p orbital can transfer to the vacant d or f orbitals of Eu^{3+} ion and gives rise to charge transfer transition. As observed in our excitation spectra of the Eu:LNO compound in Fig. 5a the excitation peak near to 292 nm might be therefore due to $O^{2-} \rightarrow Eu^{3+}$ charge transfer transition. For, Eu^{3+} at Li-site there is no matching of the electronic states of the vacant p orbital of oxygen with that of the d and f orbital of Eu^{3+} ions. Therefore, the $O^{2-} \rightarrow Eu^{3+}$ charge transfer transition in Fig. 5a might be attributed to Eu^{3+} ion occupying the Nb-site.

The various defect formation energies of LNO is given by

$$E_f{}^q = E_{defect}{}^q - E_{perfect} - \sum_\alpha n_\alpha \mu_\alpha + q_i \mu_e + dE \quad (4)$$

where $E_{defect}{}^q$ and $E_{perfect}$ represents the DFT(GGA) calculated total energies of the system (for both pure and defect related system), n_α = number of added/removed atoms, μ_α = chemical potential of the added/removed species α, q_i = effective charge on the defect and $\mu_e = E_{VBM} + \varepsilon_F$, where E_{VBM} = energy of the valence band maximum (VBM) and ε_F = electron chemical potential above the VBM. The interactions of the defect charges with their periodic images is corrected through dE employing a Madelung correction which was proposed by Leslie and Gillan[46] using dielectric constant observed experimentally.[47]

The variation of DFT calculated defect formation energies of O, Li and Nb in various charge states in the dilute limit as

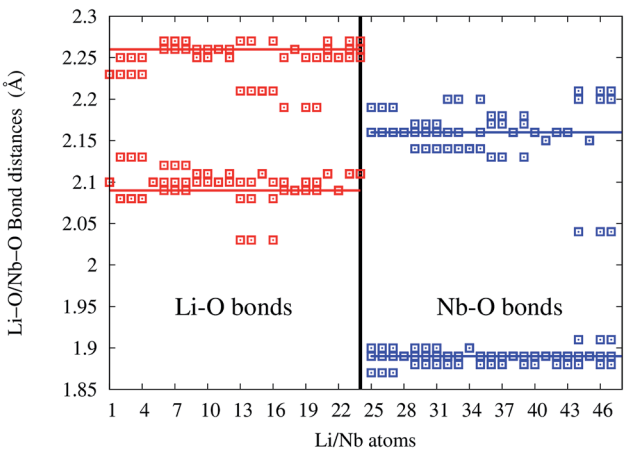

Fig. 16 Li–O and Nb–O bond-length distribution in Eu:LNO at Nb-site. Solid red and blue lines are the Li–O and Nb–O bond-lengths in undoped $LiNbO_3$.

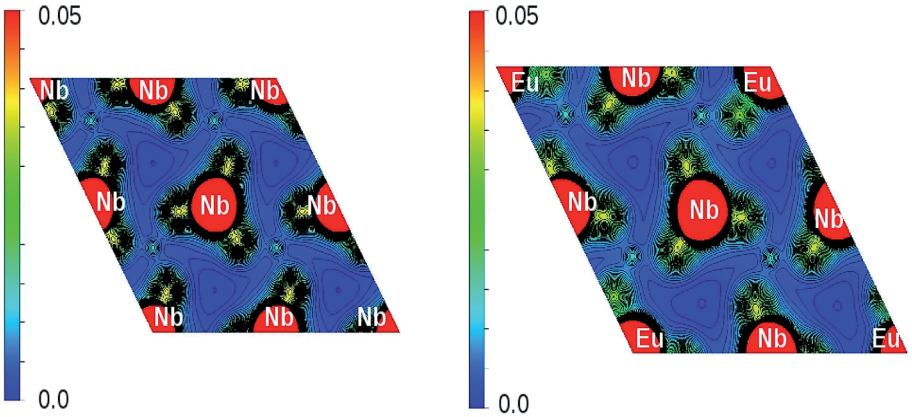

Fig. 17 Charge density distribution (in e Å^{-3}) plot on (001) plane of LNO (left panel) and Eu:LNO (right panel).

a function of Fermi energy is shown in Fig. 15 (left panel). From the DFT calculated formation energies for different vacancies, it can be said that in comparison to V_O^{1+} and V_O^0, the formation energies V_O^{2+} defects are low in the 0 to 2.4 eV range (in E_F–E_V scale) near the valence band. Thus oxygen vacancies may behave as n-type defect and to donate electrons. Similarly, we can say that V_O^{1+} defect are favored to be formed in the 2.4 to 3.0 eV (in E_F–E_V scale) and beyond this range V_O^0 defects are favored to be formed. The electronic band-gap of $LiNbO_3$ is 3.24 eV observed from the present DFT-GGA calculation.

Three charge-state transition levels as observed from present DFT calculation are shown in Fig. 15 (right panel) and they are a deep donor level ε (+2/+1) at 2.4 eV (516 nm), a deep donor level ε (+1/0) at 3.0 eV (413 nm) and another level ε (Li^{1-}/Nb^{5-}) at 2.2 eV (563 nm). Here we have defined the impurity levels as the charge-state transition levels (ε (q_1/q_2), from charge q_1 to q_2) and we have considered the Fermi level locations where different defect states with different charges have the same formation energy. These charge-state transition levels with respect to the host referred binding energies (HRBE) are shown in a conventional diagram on the right hand side of Fig. 14. We have observed similar emission bands at similar wavelength region in undoped LNO. Hence, the transition between different oxygen vacancies might be responsible for those emissions.

In order to determine energy preferences to incorporate Eu in LNO lattices at Li and Nb sites, the incorporation energies were calculated. The incorporation energy of a Eu atom at a defect site, for example Eu at an lithium vacancy site, is given by,

$$E[\mathrm{Eu}(V_{\mathrm{Li}})] = E[\mathrm{Eu_{Li}Li}_{n-1}\mathrm{Nb}_n\mathrm{O}_{3n}] - E[\mathrm{Li}_{n-1}\mathrm{Nb}_n\mathrm{O}_{3n}] - E[\mathrm{Eu}] \quad (5)$$

where $E[\mathrm{Eu_{Li}Li}_{n-1}\mathrm{Nb}_n\mathrm{O}_{3n}]$ is the total energy of the supercell containing a Eu atom at an lithium vacancy. $E[\mathrm{Li}_{n-1}\mathrm{Nb}_n\mathrm{O}_{3n}]$ and E[Eu] is the total energy of the cell containing an lithium vacancy and the energy of Eu metal in its bcc ground state. Based on our DFT calculations the incorporation energies of Eu in Li and Nb vacancy site is −5.17 and −11.68 eV, respectively. The incorporation energies were calculated with 120 atom (2 × 2 × 2 supercell) cell with one Li/Nb vacancy and one Eu atom placed at Li/Nb vacancy site. Based on this assessment incorporation of Eu is energetically favorable in Nb site compared to Li site. We have also proved earlier that the $O^{2-} \rightarrow Eu^{3+}$ charge transfer excitation for Eu^{3+} doped LNO in Fig. 5a is due to Eu^{3+} ion occupying the Nb-site only, which indicates that substitution at Li-site is more favorable.

In undoped LNO, Li/Nb atoms forms LiO_6/NbO_6 polyhedra at distances 2.09 (3 bonds), 2.26 Å (3 bonds)/1.89 (3 bonds), 2.16 Å (3 bonds) shown as solid horizontal lines in bond-length distribution curve. In Eu:LNO (Eu in Nb site), Li–O and Nb–O bond-lengths are distributed in the range 2.02–2.13, 2.17–2.28 Å and 1.86–1.92, 2.02–2.23 Å, respectively (as shown in Fig. 16).

The x-axis of Fig. 16 shows the Li (24 atoms) and Nb (23 atoms) atoms in the 120 atoms supercell. Based on this analysis, it is evident that Eu-doping distort the LNO lattice. Similar observation can also be made from the contour plots of pure LNO and Eu:LNO. The distorted charge density contours can be identified around the Eu atoms in the (001) plane in Fig. 17. This structural distortion is responsible for the enhancement of ferroelectric properties in LNO compound.

4. Conclusion

Multifunctional LNO and Eu:LNO_3 compounds are synthesised through solid state method followed by their characterisation with XRD and FTIR. Photoluminescence study reveals that the undoped compound is a blue light emitting material, while upon doping with Eu^{3+}, the compound turned to be both as blue and red emitting phosphor materials, depending upon the excitation wavelength. The blue emission from the host is attributed to several defect canters which creates many electronic states inside the band gap. Using TRES study we have isolated the defect related emissions. Both undoped and Eu^{3+} doped compounds are found to show ferroelectric behaviour, however, the remnant polarization has been increased for Eu^{3+} doped compound with higher leakage current density. Since the ferroelectric properties in LNO are originated due to structural distortion, the enhancement of remnant polarization was due to more distortion induced by the Eu^{3+} dopant ion, which has larger ionic radii than host cations and different charge. The

fact that the structure became more distorted was also supported by the fact that the point symmetry calculated from stark-splitting pattern of the characteristics emission of Eu^{3+} ions was found to be changed from the reported C_{6v} for undoped to D_3 when Eu^{3+} ions are doped. From DFT based theoretical calculation, various electronic states originated from different defect centers are found to exist inside the band gap of the material, which results in the multicolor host emission. The charge transfer transition has also been explained by DFT calculation. It was also observed that Eu^{3+} ions energetically favor to occupy the Nb site. Further from DFT calculation it was observed that there is a change in the structural parameters due to structural distortion when Eu^{3+} is doped, which justified the fact that the structural distortion lead to tuning of the electrical properties.

Conflicts of interest

All authors are hereby declared that there is no conflict of interest.

Acknowledgements

The authors thank Dr Bal Govind Vats FCD, BARC for the FTIR measurements. The work is fully funded by our own institute *i.e.* BARC. No external funding agency was involved.

References

1 L. T. Canham, *Appl. Phys. Lett.*, 1990, **57**, 1046–1048.
2 H. Ohno, *Science*, 1998, **281**, 951–956.
3 X. S. Wang, C. N. Xu, H. Yamada, K. Nishikubo and X. G. Zheng, *Adv. Mater.*, 2005, **17**, 1254.
4 H. Zou, D. F. Peng, G. H. Wu, X. S. Wang, D. H. Bao, J. Li, Y. X. Li and X. Yao, *J. Appl. Phys.*, 2013, **114**, 073103.
5 H. Q. Sun, D. F. Peng, X. S. Wang, M. M. Tang, Q. W. Zhang and X. Yao, *J. Appl. Phys.*, 2011, **110**, 016102.
6 X. Wang, D. Peng, B. Huang, C. Pan and Z. L. Wang, *Nano Energy*, 2019, **55**, 389–400.
7 G. F. Teixeira, E. S. Junior and A. Z. Simões, *CrystEngComm*, 2017, **19**, 4378.
8 (*a*) H. Wei, H. Wang, Y. Xia, D. Cui, Y. Shi, M. Dong, C. Liu, T. Ding, J. Zhang, Y. Ma, N. Wang, Z. Wang, Y. Sun, R. Wei and Z. Guo, *J. Mater. Chem. C*, 2018, **6**, 12446–12467; (*b*) Y. Zhang, X. Pan and Z. Wang, *RSC Adv.*, 2015, **5**, 20453.
9 J. H. Jung, M. Lee and J. I. Hong, *ACS Nano*, 2011, **5**, 10041.
10 S. M. Neumayer, A. V. Ievlev, L. Collins, R. Vasudevan, M. A. Baghban, O. Ovchinnikova, S. Jesse, K. Gallo, B. J. Rodriguez and S. V. Kalinin, *ACS Appl. Mater. Interfaces*, 2018, **10**(34), 29153–29160.
11 M. Friedrich, W. G. Schmidt, A. Schindlmayr and S. Sanna, *Phys. Rev. Mater.*, 2017, **1**, 034401.
12 O. F. Schirmjzr, O. Thiemann and M. W. Hlecke, *J. Phys. Chem. Solids*, 1991, **52**, 185–200.
13 H. Megaw and C. N. W. Darlington, *Acta Crystallogr., Sect. A: Cryst. Phys., Diffr., Theor. Gen. Crystallogr.*, 1975, **31**, 161.
14 H. J. Xiang, *Phys. Rev. B: Condens. Matter Mater. Phys.*, 2014, **90**, 094108.
15 K. E. Johnston, C. C. Tang, J. E. Parker, K. S. Knight, P. Lightfoot and S. E. Ashbrook, *J. Am. Chem. Soc.*, 2010, **132**(25), 8732.
16 B. C. Grabmaier, W. Wersing and W. Koestler, *J. Cryst. Growth*, 1991, **110**, 339–347.
17 C. Wang, J. Sun, W. Ni, B. Yue, F. Hong, H. Liu and Z. Cheng, *J. Am. Ceram. Soc.*, 2019, **102**, 6705–6712.
18 T. Volk, L. Ivleva, P. Lykov, N. Polozkov, V. Salobutin, R. Pankrath and M. Wöhlecke, *Opt. Mater.*, 2001, **18**(1), 179–182.
19 A. Brenier, *Opt. Commun.*, 1996, **129**, 57.
20 G. Foulon, M. Ferriol, A. Brenier, M. T. Cohen-Adad and G. Boulon, *Chem. Phys. Lett.*, 1995, **245**, 555.
21 E. Montoya, J. Capmany, L. E. Bausá, T. Kellner, A. Diening and G. Huber, *Appl. Phys. Lett.*, 1999, **74**, 3113.
22 I. Dohnke, B. Trusch, D. Klimm and J. Hulliger, *J. Phys. Chem. Solids*, 2004, **65**, 1297.
23 K. Sanyal, N. Pathak, A. K. Yadav, B. Kanrar, R. M. Kadam, S. N. Jha, D. Bhattacharya and N. L. Misra, *Dalton Trans.*, 2016, **45**, 7650–7664.
24 S. K. Gupta, N. Pathak and R. M. Kadam, *J. Lumin.*, 2016, **169**, 106–114.
25 S. K. Gupta, P. S. Ghoshb, N. Pathak and R. M. Kadam, *RSC Adv.*, 2016, **6**, 42923–42932.
26 S. K. Gupta, P. S. Ghosh, C. Reghukumar, N. Pathak and R. M. Kadam, *RSC Adv.*, 2016, **6**, 44908–44920.
27 J. E. Muñoz Santiuste, B. Macalik and J. García Solé, *Phys. Rev. B: Condens. Matter Mater. Phys.*, 1993, **47**, 88.
28 D. Hreniaka, A. Speghini, M. Bettinelli and W. Streka, *J. Lumin.*, 2006, **119–120**, 219–223.
29 D. Hreniak and W. Strek, *Appl. Phys. Lett.*, 2006, **88**, 161118.
30 (*a*) N. Pathak, S. K. Gupta, P. S. Ghosh, A. Arya and V. Natarajan, *RSC Adv.*, 2015, **5**(23), 17501–17513; (*b*) S. K. Gupta, N. Pathak, P. S. Ghosh, B. Rajeshwari, V. Natarajan and R. M. Kadam, *J. Magn. Magn. Mater.*, 2015, **391**, 101–107; (*c*) S. K. Gupta, N. Pathak, P. S. Ghosh and R. M. Kadam, *J. Alloys Compd.*, 2017, **695**, 337–343.
31 (*a*) R. Phatak, N. Pathak, S. Muhammed, S. K. Sali and A. Das, *ChemPlusChem*, 2018, **83**, 1144–1152; (*b*) R. Phatak, N. Pathak, S. Muhammed, A. Das and S. K. Sali, *J. Am. Ceram. Soc.*, 2020, **103**, 2617–2629.
32 (*a*) N. Pathak, P. S. Ghosh, S. Saxena, D. Dutta, A. K. Yadav and D. Bhattacharyya, *Inorg. Chem.*, 2018, **57**(7), 3963–3982; (*b*) N. Pathak, P. S. Ghosh, S. K. Gupta, S. Mukherjee, R. M. Kadam and A. Arya, *J. Phys. Chem. C*, 2016, **120**(7), 4016–4031; (*c*) N. Pathak, P. S. Ghosh, S. K. Gupta, R. M. Kadam and A. Arya, *RSC Adv.*, 2016, **6**, 96398–96415.
33 (*a*) N. Pathak, S. Mukherjee, D. Das, D. Dutta, S. Dash and R. M. Kadam, *J. Mater. Chem. C*, 2020, **8**, 7149–7161; (*b*) D. Hebbar, K. S. Choudhari, N. Pathak, S. A. Shivashankar and S. D. Kulkarni, *J. Alloys Compd.*, 2018, **768**, 676–685; (*c*) P. Das, N. Pathak, B. Sanyal, S. Dash and R. M. Kadam, *J. Alloys Compd.*, 2019, **810**, 1519062.
34 R. S. Weis and T. K. Gaylord, *Appl. Phys. A: Solids Surf.*, 1985, **37**, 191–203.

35 X. Y. Chen, W. Zhao, R. E. Cook and G. K. Liu, *Phys. Rev. B: Condens. Matter Mater. Phys.*, 2004, **70**(20), 2051221–2051229.
36 X. Y. Chen and G. K. Liu, *J. Solid State Chem.*, 2005, **178**(2), 419–428.
37 S. V. Eliseevaa and J. C. G. Bunzli, *Chem. Soc. Rev.*, 2010, **39**, 189.
38 Q. Ju, Y. Liu, R. Li, L. Liu, W. Luo and X. Chen, *J. Phys. Chem. C*, 2009, **113**, 2309.
39 L. Hao, Y. Li, J. Zhu, Z. Wu, F. Long, X. Liu and W. Zhang, *J. Alloys Compd.*, 2014, **590**, 205–209.
40 M. Sumets, *Lithium Niobate-Based Heterostructures*, IOP Publishing, 2018, DOI: 10.1088/978-0-7503-1729-0ch1.
41 M. P. Sumets, V. A. Dybov and V. M. Levlev, *Inorg. Mater.*, 2017, **53**, 1361.
42 K. Parlinski, Z. Q. Li and Y. Kawazoe, *Phys. Rev. B: Condens. Matter Mater. Phys.*, 2000, **61**, 272.
43 H. Boysen and F. Altorfer, *Acta Crystallogr., Sect. B: Struct. Sci.*, 1994, **50**, 405.
44 M. Veithen and P. Ghosez, *Phys. Rev. B: Condens. Matter Mater. Phys.*, 2002, **65**, 214302.
45 W. G. Schmidt, M. Albrecht, S. Wippermann, S. Blankenburg, E. Rauls, F. Fuchs, C. Rödl, J. Furthmüller and A. Hermann, *Phys. Rev. B: Condens. Matter Mater. Phys.*, 2008, **77**, 035106.
46 M. Leslie and M. J. Gillan, *J. Phys. C: Solid State Phys.*, 1985, **18**, 973–982.
47 A. Mansingh and A. Dhar, *J. Phys. D: Appl. Phys.*, 1985, **18**, 2059–2071.